UC Berkeley

Title

Exchange Coupling Determines Metal-Dependent Efficiency for Iron- and Cobalt-Catalyzed Photochemical CO2 Reduction

Authors

De La Torre, Patricia

Derrick, Jeffrey S

Snider, Andrew

et al.

Peer reviewed

Exchange Coupling Determines Metal-Dependent Efficiency for Iron- and Cobalt-Catalyzed Photochemical CO₂ Reduction

Patricia De La Torre,[a,b] Jeffrey S. Derrick,[a,b] Andrew Snider,[a] Peter T. Smith,[a,b] Matthias Loipersberger,[a] Martin Head-Gordon,[a,b] and Christopher J. Chang[a,b,c]*

[a] Department of Chemistry, University of California, Berkeley, California 94720, United States

[b] Chemical Sciences Division, Lawrence Berkeley National Laboratory, Berkeley, California 94720, United States

[c] Department of Molecular and Cell Biology, University of California, Berkeley, California 94720, United States

*Corresponding author: chrischang@berkeley.edu

Table of Contents Synopsis (75 words)

We present an experimental and computational study of iron and cobalt complexes bearing the redox non-innocent ligand tpyPY2Me for catalyzing photochemical CO_2 reduction. Metal-ligand exchange coupling drives facile two-electron reduction of the iron system to an open-shell singlet configuration with a doubly reduced ligand, enabling highly selective and active reduction of CO_2 to CO. In contrast, cobalt reduction proceeds by two single-electron steps, resulting in an open-shell doublet with markedly diminished catalytic activity and stability.

Table of Contents Graphic
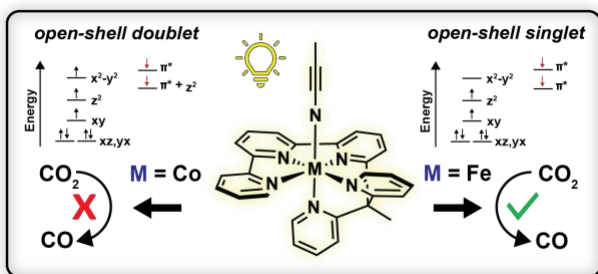
ABSTRACT: Catalyst platforms that promote multielectron charge delocalization offer an attractive approach to achieving the CO_2 reduction reaction (CO_2RR) with selectivity over the competing hydrogen evolution reaction (HER). Here, we show the importance of metal-ligand exchange coupling as an example of charge delocalization that can determine efficiency for photocatalytic CO_2RR. A comparative evaluation of iron and cobalt complexes supported by the redox-active ligand tpyPY2Me establishes that the two-electron reduction of $[Co(tpyPY2Me)]^{2+}$ ($\mathbf{[Co]^{2+}}$) occurs at potentials 770 mV more negative than the $[Fe(tpyPY2Me)]^{2+}$ ($\mathbf{[Fe]^{2+}}$) analog by maximizing exchange coupling in the latter compound. The positive shift in reduction potential promoted by metal-ligand exchange coupling drives $\mathbf{[Fe]^{2+}}$ to be among the most active and selective molecular catalysts for photochemical CO_2RR reported to date, maintaining up to 99% CO product selectivity with total turnover numbers (TON) and initial turnover frequencies (TOF) exceeding 30,000 and 900 min^{-1}, respectively. In contrast, $\mathbf{[Co]^{2+}}$ shows much lower CO_2RR activity, reaching only ca. 600 TON at 83% CO product selectivity under similar conditions accompanied by rapid catalyst decomposition. Spin density plots of the two-electron reduced $\mathbf{[Co]^0}$ complex implicate a paramagnetic open-shell doublet ground state compared to the diamagnetic open-shell singlet ground state of reduced $\mathbf{[Fe]^0}$, rationalizing the observed negative shift in two-electron reduction potentials from the $\mathbf{[M]^{2+}}$ species and lowered CO_2RR efficiency for the cobalt complex relative to its iron congener. This work emphasizes the contributions of multielectron metal-ligand exchange coupling in promoting effective CO_2RR and provides a starting point for the broader incorporation of this strategy in catalyst design.

INTRODUCTION

The selective and efficient transformation of carbon dioxide into value-added products offers a sustainable approach to generate fuels, foods, materials, and medicines from renewable feedstocks.[1-4] Artificial photosynthesis is a potentially powerful strategy towards achieving this goal,[5-15] where concept transfer from natural photosynthesis can be incorporated into synthetic systems capable of reducing CO_2 through light-initiated proton- and electron-transfer reactions. In this context, homogeneous artificial photosynthesis platforms offer the capacity to tune system performance using well-defined components, including the molecular catalyst, photosensitizer with an energy-matched reduction potential, and sacrificial electron donor with maximum quenching efficiency.[11, 16-22] Indeed, recent advances in molecular photocatalysis for the carbon dioxide reduction reaction (CO_2RR) include metal-dependent enhancement of organic photosensitizers,[20, 23]the use of hydrogen bonding,[24] electrostatic,[14,25, 26] or covalent[27] interactions between photosensitizer and catalyst to improve electron transfer, and additives to increase CO_2 solubility.[28-32]

In terms of new catalyst design, first-row transition metal complexes supported by polypyridyl ligand frameworks[30, 32-52] have emerged as privileged scaffolds for CO_2RR. For example, we recently found that strong metal-ligand exchange coupling between an iron center and pentadentate polypyridyl ligand (tpyPY2Me) promotes its facile two-electron reduction to yield a reduced diamagnetic complex, [Fe(tpyPY2Me)] (**[Fe]^0**), which we assigned to an open-shell singlet ground state that is composed of an intermediate-spin Fe^{2+} center antiferromagnetically coupled to a doubly-reduced triplet tpyPY2Me ligand.[44] The metal-ligand cooperativity in this Fe^{2+} complex leads to a 640 mV positive shift in the first two ligand-centered reductions relative to the Zn^{2+} analog, enabling catalysis of electrochemical CO_2RR at low

4

overpotentials with high selectivity over the hydrogen evolution reaction (HER) by delocalizing electron density beyond the primary metal center. Moreover, the analogous nickel tpyPY2Me complex, [Ni(tpyPY2Me)]$^{2+}$ (**[Ni]$^{2+}$**), has found application as an efficient redox mediator for controlling radical pathways by ligand-centered redox reactivity.[53]

Against this backdrop, we sought to expand the reactivity of metal tpyPY2Me complexes to photochemical CO_2RR. Considering the precedent for cobalt-based CO_2RR catalysts,[11, 18, 23, 39, 54-57] we now report a comparative study between iron and cobalt tpyPY2Me complexes for photochemical CO_2RR, including synthesis and characterization of the novel cobalt tpyPY2Me complex, [Co(tpyPY2Me)]$^{2+}$ (**[Co]$^{2+}$**). We find that electron count makes a substantial contribution to metal-ligand cooperativity and redox behavior in these transition metal tpyPY2Me complexes. In contrast to the **[Fe]$^{2+}$** complex, where the first two single-electron, ligand-based reduction waves are virtually superimposable, electrochemical characterization of **[Co]$^{2+}$** shows a 1.39 V separation between the first and second redox processes where two-electron reduction potential of **[Co]$^{2+}$** is shifted negatively by 770 mV compared to **[Fe]$^{2+}$**. This marked difference in multielectron redox behavior correlates with observed photocatalytic CO_2RR reactivity. Indeed, the **[Fe]$^{2+}$** complex is compatible with photosensitizers spanning reduction potentials over a range of 1 V and can promote efficient light-driven CO_2 reduction with high activity and selectivity, achieving up to 99% CO product selectivity with total turnover numbers (TON) and initial turnover frequencies (TOF) exceeding 30,000 and 900 min^{-1}, respectively, whereas the **[Co]$^{2+}$** complex shows much lower CO_2RR activity under similar conditions (ca. 600 TON, 83% CO product selectivity). Density functional theory (DFT) calculations support these experimental findings by suggesting that the first reduction of **[Co]$^{2+}$** to **[Co]$^+$** is metal-centered, and that the second reduction to **[Co]^0** is accompanied by a significant rearrangement of electrons that enforces exchange coupling

between a formal Co^{2+} center and a two-electron reduced ligand, resulting in a paramagnetic open-shell doublet. This electronic structure differs from the two-electron reduction of **[Fe]$^{2+}$**, resulting in a diamagnetic, open-shell singlet **[Fe]^0** complex between a formal Fe^{2+} center and a two-electron reduced ligand. As such, we attribute the superior catalytic performance of the iron system over the cobalt congener to the more stable electronic configuration for reduced **[Fe]^0** vs **[Co]^0** driven by this metal-ligand exchange coupling. Taken together, these data highlight the importance of metal-ligand redox cooperativity in developing efficient CO$_2$RR catalysts, which can be carried forward as a design principle for a broader range of multielectron redox transformations of interest.
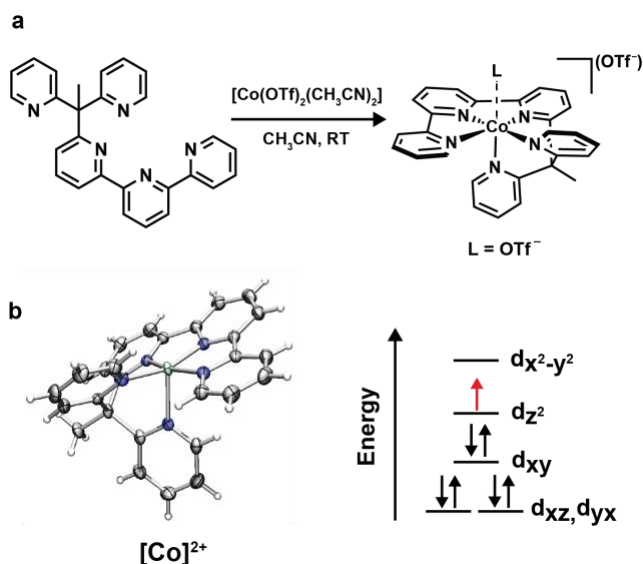

Figure 1. a) Synthetic scheme and (b) X-ray crystal structure for the [Co(tpyPY2Me)]$^{2+}$ (**[Co]$^{2+}$**) complex, with its simplified crystal field splitting diagram.

RESULTS AND DISCUSSION

Synthesis and Structural Characterization of the [Co(tpyPY2Me)]$^{2+}$ Complex. The [Co(tpyPY2Me)]$^{2+}$ complex (**[Co]$^{2+}$**) was obtained in nearly quantitative yield by stirring the

ligand tpyPY2Me with an equimolar amount of the cobalt precursor [Co(OTf)$_2$(CH$_3$CN)$_2$] in dry CH$_3$CN at room temperature for 12 hours (Figure 1a). Diffraction quality crystals for **[Co]$^{2+}$** were obtained by slow vapor diffusion of diethyl ether into a saturated CH$_3$CN solution. The crystal structure of **[Co]$^{2+}$** (Figure 1b) shows its connectivity as a five-coordinate square pyramidal complex, analogous to the previously reported [Zn(tpyPY2Me)]$^{2+}$ analog.[44] Co–N$_{tpy}$ bond lengths range from 1.8975(17) to 1.9610(18) Å, consistent with a low-spin Co^{2+} configuration, exhibiting shorter bond lengths compared to high-spin Co d^7 complexes with a similar coordination environment.[58, 59] Analysis of the C$_{py}$–C$_{py}$ bonds connecting the terpyridine moiety and the C–N bonds within the terpyridine chelate rings (with average bond lengths of 1.471 and 1.356 Å, respectively) suggest that the ground state of **[Co]$^{2+}$** bears a neutral tpyPY2Me ligand and a Co^{2+} metal center[60]; this assignment was supported by an effective magnetic moment of 1.8 μB determined by the Evans' method (Figure 1b, S2).

Electrochemical Characterization Reveals Differences in Redox Behavior, Catalytic Efficiency, and Reductive Stability Between [Co(tpyPY2Me)]$^{2+}$ and [Fe(tpyPY2Me)]$^{2+}$ for CO$_2$RR. As a starting point to compare the redox properties of the **[Co]$^{2+}$** and **[Fe]$^{2+}$** complexes, we measured the cyclic voltammogram (CV) of **[Co]$^{2+}$** under an argon atmosphere. The CV shows a quasi-reversible wave at E$_{1/2}$ = +0.023 V vs Fc$^{0/+}$ and three reversible waves at E$_{1/2}$ = –0.81, –2.20, –2.34 V vs Fc$^{0/+}$ (Figure 2). Currents for all redox waves vary linearly with the square root of the scan rate, indicative of diffusion-controlled processes (Figure S1). The first wave at E$_{1/2}$ = +0.02 V vs Fc$^{0/+}$ is assigned to a Co$^{2+/3+}$ oxidation, as its quasi-reversible nature is characteristic for cobalt complexes exhibiting low/high spin transitions coupled to a redox process.[61-64] The second wave is assigned to a Co$^{2+/+}$ reduction process, which is positively shifted by +0.39 V
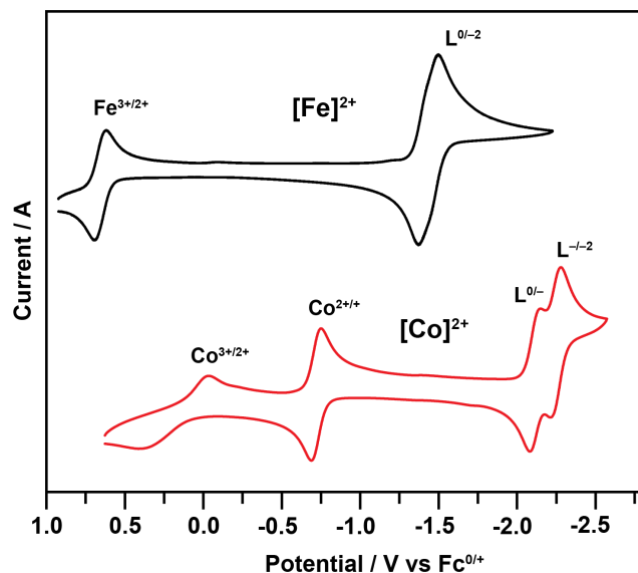
Figure 2. Cyclic voltammograms of **[Fe]$^{2+}$** (black) and **[Co]$^{2+}$** (red). Conditions: 1 mM [M(tpyPY2Me)]$^{2+}$ complex, 0.1 M NBu$_4$PF$_6$ in CH$_3$CN under Ar atmosphere.

compared to the Co^{2+} complex of bpy2PYMe, and consistent with an observed pattern of stabilization with increasing conjugation in pyridine-based redox active ligands.[64] We assign the latter two waves at E$_{1/2}$ = –2.20 and –2.34 V vs Fc$^{0/+}$ as ligand-centered reductions by comparison to the [Zn(tpyPY2Me)]$^{2+}$ analog bearing a redox-silent Zn^{2+} center, whose first two ligand-centered redox processes lie between –1.56 and –2.41 V vs Fc$^{0/+}$.[44] This electrochemical behavior contrasts with the two closely-spaced ligand-dependent reductions in [Fe]$^{2+}$ centered at –1.43 V vs Fc$^{0/+}$ [44] (Figure 2). As such, the change from iron to cobalt shifts the first two reductions in a negative direction by 770 mV, indicating a significant difference in the thermodynamic stability of metal-ligand electronic coupling in the reduced cobalt complex compared to its iron congener.

We next moved on to screen **[Co]$^{2+}$** for electrochemical CO$_2$RR reactivity. Upon addition of CO$_2$, we observe a current enhancement, which increases further upon the addition of 0.1 M phenol as an acid source (Figure 3a). Under an Ar atmosphere, the addition of 0.1 M phenol results

in a larger relative current enhancement, indicative of HER reactivity (Figure 3b). We then measured product selectivity and long-term catalyst stability via controlled potential electrolysis (CPE) experiments conducted at various applied potentials. Initially, we used glassy carbon (GC) as a working electrode for CPE experiments; however, the current density asymptotically decays within the first 50 seconds at the selected potentials (Figure S3a). CVs recorded before and immediately after electrolysis show a total loss in current response; upon polishing the GC electrode after electrolysis and resubmerging in the same electrolysis cell, the voltammograms show recovery of the same pre-electrolysis wave (Figure S3c). This behavior is indicative of catalyst deposition onto the working electrode, resulting in an inactive film that limits charge transfer during the electrolysis experiment. To limit this deposition, we turned to the use of reticulated vitreous carbon (RVC) foam as a carbon-based electrode with higher surface area for further electrolysis experiments. Use of RVC foam led to a modest enhancement in the stability and enabled more charge to be passed during the electrolysis experiment (Figure S3d, e). At an applied potential of -2.09 vs $Fc^{0/+}$ under a CO_2 atmosphere in the presence of 0.1 M phenol, $[Co]^{2+}$
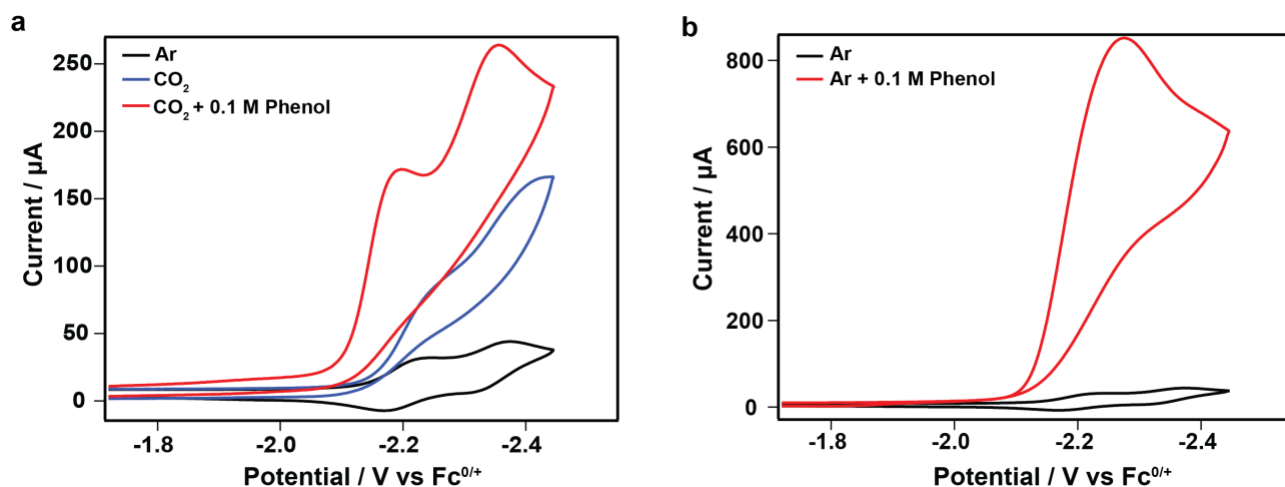

Figure 3. Cyclic voltammograms showing catalytic responses upon addition of 0.1 M phenol to $[Co]^{2+}$ (a) under CO_2 or (b) Ar atmosphere. Conditions: 1 mM $[Co]^{2+}$ in 0.1 M NBu_4PF_6/CH_3CN.

achieved 64% faradaic efficiency for CO formation (Table S1). During CPE experiments with the RVC working electrode, we observed a color change in the electrolyte that was not observed when the GC working electrode was used, where the pale orange-colored solution characteristic of $[Co]^{2+}$ converted to a dark red purple-colored solution. We speculate that this species is most likely the two-electron reduced species, $[Co]^0$, based on a similar color change observed for the chemical reduction of $[Fe]^{2+}$ to $[Fe]^0$ using decamethylcobaltocene.[44] We have not yet been successful in isolating the reduced cobalt species owing to its redox instability, but its appearance in bulk solution suggests that it contributes to the lower Faradaic efficiency and electrochemical stability observed for the cobalt catalyst relative to the iron analog.

Evaluation of $[Co(tpyPY2Me)]^{2+}$ as a Catalyst for Photochemical CO₂RR. Building upon these electrochemical results, we reasoned that moving to photochemical CO₂RR would enable lower catalyst loading (1 mM for electrolysis to 2 μM for photolysis, *vide infra*) to mitigate unproductive $[Co]^0$ accumulation by dispersing it in solution as opposed to concentrating the reduced species at the electrode double layer. Indeed, in a photocatalytic system, electron transfer operates via the bimolecular reaction of the catalyst with a photosensitizer; thus, we expected improved catalyst stability relative to the electrolysis experiments. As a starting point, we evaluated $[Co]^{2+}$ as a catalyst for photochemical CO₂RR. In a typical experiment, 2 μM $[Co]^{2+}$ was added to a CO₂-saturated CH₃CN solution containing 200 μM photosensitizer, 50 mM triethylamine (TEA) as a sacrificial electron donor, and 1 M phenol as a proton source. Reactions

were irradiated in 1-hour intervals using a blue LED light source. Multiple photosensitizers were chosen for screening owing to their close energy match to reduction waves of **[Co]²⁺**, including [Ru(bpy)₃]²⁺ (**RuPS**, $E^0 = -1.71$ V vs $Fc^{0/+}$), as well as the iridium complexes [Ir(dFCF₃ppy)₂(dtbbpy)]⁺ (**IrPS-1**, $E^0 = -2.39$ V vs $Fc^{0/+}$) and Ir(ppy)₃ (**IrPS-2**, $E^0 = -2.61$ V vs $Fc^{0/+}$) (Figure 4a). Results of photochemical CO₂RR screening studies show some improvements and similarities in activity trends compared to electrochemical CO₂RR experiments (Figure S4, Table S2). The average activity of the **IrPS-1** system over a 15-hour period shows that in the first hour, CO₂ reduction is 93% selective for CO with an average turnover number (TON) of 120. Data
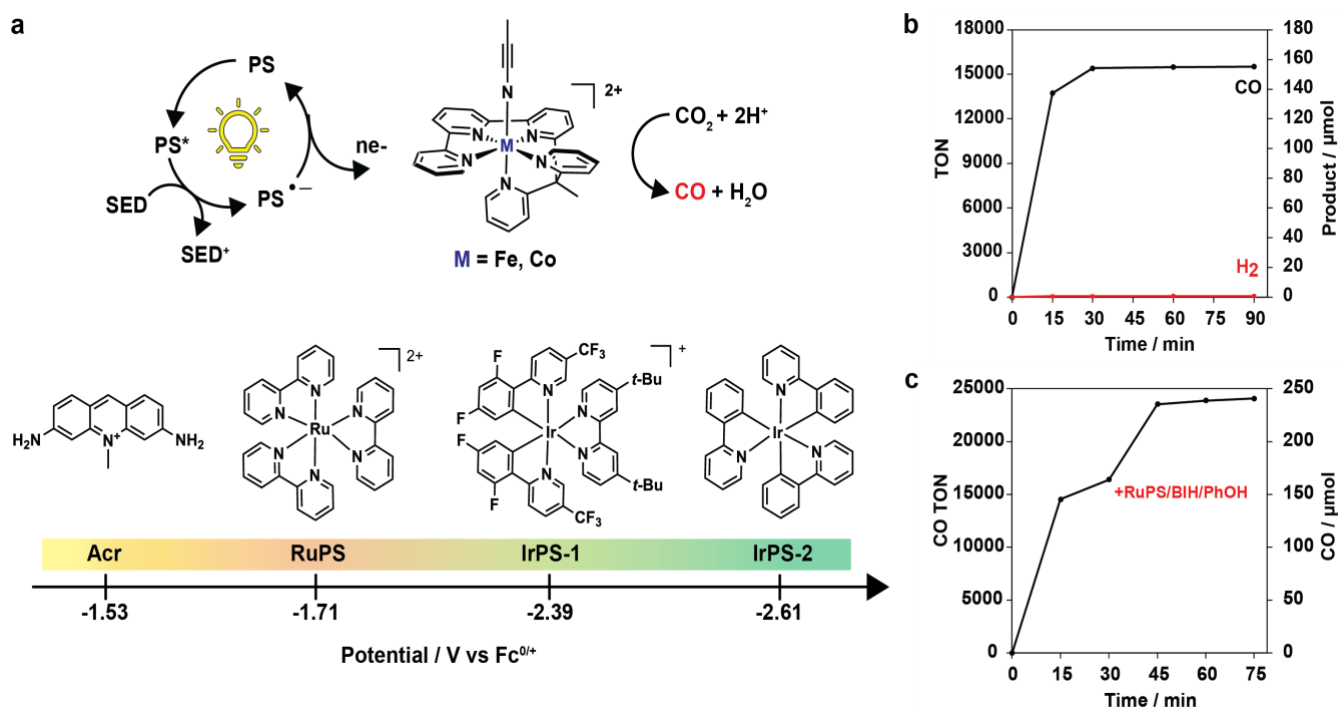
Figure 4. (a) Photochemical CO₂ reduction reactions catalyzed by iron and cobalt tpyPy2Me complexes, **[Fe]²⁺** and **[Co]²⁺**, using **Acr**, **RuPS**, **IrPS-1**, and **IrPS-2** as photosensitizers with increasing driving forces for reduction. (b) Photocatalytic activity of **[Fe]²⁺** over 90 minutes and (c) with replenishing the photosensitizer, sacrificial electron donor, and proton source every 30 minutes. Conditions: 2 μM **[Fe]²⁺**, 200 μM **RuPS**, 100 mM BIH, 1 M Phenol in CO₂-saturated CH₃CN solution.

collected at subsequent timepoints show a marked drop in activity as well as a loss of CO_2RR selectivity down to 50-57% CO product due to increased HER. We hypothesized that the modest observed CO_2RR activity may be a consequence of inefficiencies in photocatalytic system design, in particular the requirement for a high concentration of acid that may participate in hydrogen bonding with the basic TEA sacrificial electron donor, which can possibly lower its quenching efficiency. We turned to 1,3-dimethyl-2-phenyl-2,3-dihydro-1H-benzo[d]imidazole (BIH) as a replacement for TEA, which has literature precedent as an excellent quencher for photocatalytic CO_2 reduction using organic, ruthenium- and iridium-based photosensitizers.[20, 39, 45, 65, 66] With 100 mM BIH, **[Co]$^{2+}$** exhibits a switch in selectivity from CO_2RR to HER using either **RuPS** or **IrPS-1** as a photosensitizer, with an average H_2 TON of 488 achieved in one hour. Lowering the BIH concentration to 50 mM improves the selectivity to 67-83% CO, with **IrPS-1** giving the highest TON of 647 in one hour of photolysis. Despite observed gains in activity and selectivity with lower BIH loading, reactions still show a loss in CO_2RR selectivity beyond the first hour, analogous to results obtained with TEA, indicating that lowering BIH loading only slowed off-pathway H_2 evolution and deactivation pathways rather than eliminating them. Indeed, dynamic light scattering experiments confirm that within 15-30 min of irradiation, **[Co]$^{2+}$** decomposes into a particulate species with sizes in the range of 100 to 1000 nm under catalytic conditions (Figure S5a), showing that photochemical CO_2RR reactivity is ultimately limited by the stability of the catalyst under reductive conditions.

[Fe(tpyPY2Me)]$^{2+}$ Shows Superior Catalytic Activity to the [Co(tpyPY2Me)]$^{2+}$ for Photochemical CO$_2$RR. We then turned our attention to **[Fe]$^{2+}$** as a catalyst for photochemical CO_2RR, anticipating that it would exhibit better activity, selectivity, and stability compared to

12

$[Co]^{2+}$ considering its two-electron reduction at more positive potentials and superior performance as an electrochemical CO_2RR catalyst. Optimization of photocatalysis in CH_3CN solution with 1 M phenol as a proton source led us to screen a range of organic and noble-metal photosensitizers compatible under these conditions. These photosensitizers include the mildly reducing organic dye Acriflavine (**Acr**, $E^0 = -1.53$ V vs $Fc^{0/+}$), whose reduction potential lies just 100 mV more negative than the catalytically relevant $[Fe]^{2+}$ reduction, as well as **RuPS** and the highly reducing **IrPS-1** and **IrPS-2** sensitizers discussed previously (Figure 4a). In a typical experiment, 2 µM $[Fe]^{2+}$ catalyst was added to a CO_2-saturated CH_3CN solution containing 200 µM photosensitizer, 100 mM BIH as a sacrificial electron donor, and 1 M phenol as a proton source. The reactions were irradiated in either 15- or 30-minute intervals using a blue LED light source. We first examined photocatalysis using the **RuPS**/BIH system; a turnover frequency (TOF) of 916 min^{-1} is reached within the first 15 minutes of the reaction, which to the best of our knowledge is the highest reported TOF value for CO_2RR driven by a molecular catalyst.[25] A plateau is reached after 30 minutes (Figure 4b), resulting in a total TON of 15,520 with 99% selectivity for CO product with negligible H_2 evolution. During this time, we observe bleaching of the photosensitizer from a bright orange to pale yellow color, indicating degradation of **RuPS**. This degradation has been reported to proceed by dissociation of bipyridine ligands from the Ru center during light irradiation.[64, 67] We confirmed that replenishing **RuPS** with BIH and phenol could partially recover activity of $[Fe]^{2+}$ after the initial plateau, resulting in a maximum TON of 24,069 for CO production after a total of 75 min (Figure 4c). Photocatalytic activity could be further amplified by lowering the catalyst loading to 0.2 µM, achieving a TON of 30,349 within 45 minutes while still producing 30 µmols of CO with 97% product selectivity (Table 1, Entry 2). Control experiments performed confirm that the catalyst, photosensitizer, sacrificial electron donor, proton source, and

CO2 are all essential for the reaction to proceed (Table 1, Entries 4-7). Moreover, in contrast to the cobalt system, dynamic light scattering (DLS) measurements of the reaction mixture before and during peak catalytic activity at 0, 15, and 30 minutes confirm that the iron system is homogeneous, with no evidence of particle formation under photocatalytic conditions (Figure S5b).

We then employed Stern-Volmer analysis for the excited state quenching of **RuPS** using BIH and **[Fe]$^{2+}$** to probe the mechanism for photocatalysis (Figure 5). The bimolecular quenching rate constants (k_q) obtained for **[Fe]$^{2+}$** (2.7 x 10^9 M^{-1}s^{-1}) and BIH (2.2 x 10^9 M^{-1}s^{-1}) are comparable, indicating that oxidative and reductive quenching mechanisms are both accessible, but we reason
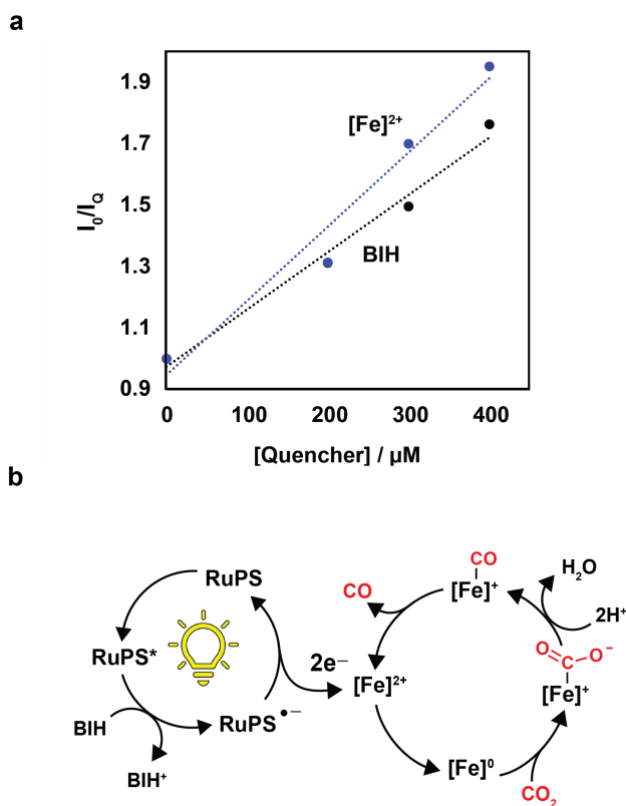

Figure 5. (a) Stern-Volmer plots for **RuPS** quenching with [Fe1]$^{2+}$ and BIH. Conditions: 50 μM **RuPS** with BIH in a CO2 saturated CH3CN solution. (b) Predicted reductive quenching mechanism for photocatalytic CO2 Reduction using **[Fe]$^{2+}$** as the catalyst, BIH as the sacrificial electron donor, and RuPS as the photosensitizer.

that the large excess of BIH used relative to $[Fe]^{2+}$ in the system will favor the reductive quenching pathway. [68] The quantum yield for CO production from the **RuPS** system with 2 µM $[Fe]^{2+}$ was determined to be Φ= 11.1% by ferrioxalate actinometry (see SI for details).

As such, we turned our attention to the water-soluble organic dye **Acr**, which has a similar redox potential to Purpurin and has been reported for photocatalytic water splitting and CO_2 reduction at 400 µM concentrations in CH_3CN/H_2O mixtures.[57, 69] The maximum solubility of **Acr** in pure CH_3CN is approximately 125 µM. The use of a less reducing photosensitizer at lower concentrations led to slower photochemical CO_2RR catalysis, with a TON of 6,710 with 100% selectivity for CO product obtained after 2 hours of photolysis. We observe a gradual decrease in activity over time, likely due to the decomposition of the photosensitizer, as evidenced by bleaching observed much like with **RuPS**. These results establish a highly selective and active noble-metal free molecular system for catalytic photochemical CO_2RR using **Acr** and $[Fe]^{2+}$ components.

Finally, we examined $[Fe]^{2+}$-catalyzed photochemical CO_2RR with the iridium-based photosensitizers **IrPS-1** and **IrPS-2** to provide a direct comparison with results obtained using $[Co]^{2+}$. In addition, Ir-C cyclometallation in these complexes provides longer photostability compared to **RuPS** and **Acr**,[70] providing an opportunity to probe contributions of photosensitizer stability to CO_2RR catalysis. Using **IrPS-1** as a photosensitizer with 2 µM $[Fe]^{2+}$ as a CO_2RR catalyst results in a TON of 12,749 with 98% selectivity for CO (Table 1, Entry 8), representing a 20-fold improvement over $[Co]^{2+}$. Lowering the catalyst concentration to 0.2 µM gives a two-fold higher TON of 28,712 but with only 81% CO selectivity (Table 1, Entry 9). Using **IrPS-2** drives the highest TON of 18,502 at 2 µM $[Fe]^{2+}$ catalyst loading conditions (Table 1, Entry 10). Interestingly, the plateau in catalytic activity observed using **IrPS-2** shows distinct behavior

compared with the one observed with **RuPS**, since the former photosensitizer is cyclometalated and should not be the source of system deactivation. Indeed, we found that for the **IrPS-2** system, introduction of additional **[Fe]$^{2+}$**, but not BIH and phenol, can enable recovery of activity (Figure S6), in contrast to the **RuPS** system where replenishing with **RuPS**/BIH/phenol can restore catalysis (Figure 4c). These results suggest that using the more reducing iridium photosensitizers can drive rapid photochemical CO$_2$RR with high selectivity for CO production but also accelerate catalyst deactivation. Key results obtained for use of **[Fe]$^{2+}$** as a photocatalyst with all four photosensitizers and control experiments using are summarized in Table 1.

Table 1. Photocatalytic activity of **[Fe]$^{2+}$** under various conditions.

Entry	TON		Product (µmol)		Selectivity (%)
	CO	H$_2$	CO	H$_2$	CO
1	15520	86	155	0.86	99
2^a	30349	1013	30	1	97
3^b	43	52	0.4	0.5	52
4^c	112	0	1.1	0	100
5^d	150	0	1.5	0	100
6^e	6	0	0	0	100
7^f	0	222	0	2.2	0
8^g	12749	163	127	1.6	98
9^h	28712	6527	28	6.5	81
10^i	18502	141	185	1.4	99
11^j	6710	0	67	0	100

Reaction conditions: Standard conditions using 2 μM **[Fe]$^{2+}$** catalyst, 200 μM **RuPS** photosensitizer, 100 mM BIH quencher, and 1 M phenol as a proton source in 5 mL of CO$_2$-saturated CH$_3$CN solution, irradiated for 90-120 minutes unless otherwise noted. [a] Using 0.2 μM catalyst. [b] Without catalyst. [c] Without **RuPS**. [d] Without BIH. [e] Without phenol. [f] Under Ar atmosphere. [g] Using 200 μM **IrPS-1** at 2 μM and [h] 0.2 μM catalyst loading. [i] Using 200 μM **IrPS-2**. [j] Using 125 μM Acriflavine (**Acr**).

Electronic Structure Calculations for Reduced Iron, Cobalt, and Nickel tpyPY2Me Complexes Show Key Differences in Metal-Ligand Exchange Coupling that Correlate with Observed Redox and Catalytic Stability. Computational predictions for the first and second reduction potentials of the **[Co]$^{2+}$** complex, modeled as [Co(tpyPY2Me)(CH$_3$CN)]$^{2+}$, were obtained using DFT calculations employing ωB97X-V functionals and CH$_3$CN solvent. DFT analysis shows the first reduction of **[Co]$^{2+}$** to **[Co]$^+$** is a metal-centered process (Figure 6, left), resulting in a singlet ground state (S = 0) and a predicted redox potential (E^0 = –0.887 V vs Fc$^{0/+}$) that is consistent with the experimental value (–0.81 V). Additional computational results from localized orbital bonding analysis (LOBA) confirm that the **[Co]$^+$** complex can be described as a formal Co$^+$ center bound to a neutral tpyPY2Me ligand. The first reduction is accompanied by the loss of the axial solvent ligand, resulting in a 5-coordinate **[Co]$^+$** complex. DFT analysis of the doubly reduced **[Co]^0** complex is consistent with the population of a ligand-based π* orbital belonging to the terpyridine fragment of the ligand (Figure 6, right). The calculated redox potential (E$_0$ = –2.22 V vs Fc$^{0/+}$) matches the experimentally determined value (E$_{1/2}$= –2.34 V) and has a calculated spin state of S = 1/2. Interestingly, the spin density plot for **[Co]^0** (Figure 6c, right) suggests that this second reduction is accompanied by significant rearrangement of electrons occupying the metal d orbitals, leading to the population of a low-lying metal-ligand (π* + d$_{z^2}$) orbital with concomitant reordering of Co-based electrons into a high-spin configuration. The

computational results suggest that the $[\text{Co}]^0$ species exists as a formal Co^{2+} center bound to $(\text{tpyPY2Me}^{\bullet\bullet})^{2-}$. Taken together, these results highlight an intriguing outcome of formal oxidation of the metal center through reduction of the overall complex, made possible via delocalized reduction events as a result of metal-ligand exchange coupling. Coordinates of the optimized structures for $[\text{Co}]^+$ and $[\text{Co}]^0$ obtained using the ωB97X-D functional are shown in tables (Table
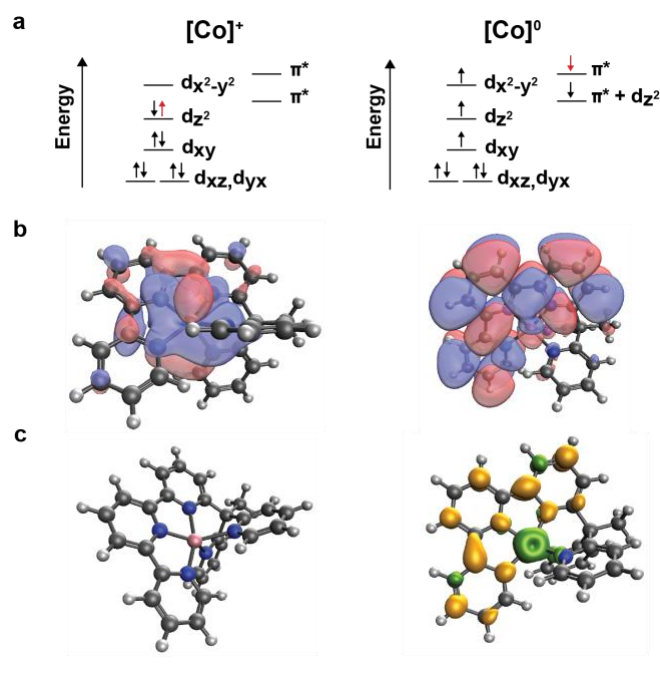
Figure 6. DFT analysis of electrochemically accessible reduced species, $[\text{Co}]^+$ and $[\text{Co}]^0$. For each reduced species, the following are shown: (a) qualitative molecular orbital diagram consistent with DFT calculations, with newly added electrons highlighted in red; (b) relevant computed MO and (c) the computed spin density plot. The DFT results show that the first reduction is cobalt-centered to generate a formal Co^+ species, whereas the second reduction is ligand-centered, leading to a substantial rearrangement of electron density resulting in restoration of a formal Co^{2+} complex with a doubly-reduced tpyPY2Me ligand.

S6,7).

The reduction pathway of $[Co]^{2+}$ contrasts with computational studies of the analogous $[Ni]^{2+}$ and $[Fe]^{2+}$ complexes.[44, 53] Figure 7 highlights how slight changes in the central metal orbitals lead to substantive changes in the metal-ligand orbital interactions and on the overall outcome of reduction events. Apart from affecting coordination number via loss of the axial solvent ligand, the molecular orbitals shown in Figure 7 show distinct differences in the type of reduction event taking place within the complexes. Indeed, in contrast to the metal-centered one-electron reduction of $[Co]^{2+}$ to $[Co]^+$ to generate a complex with a formally reduced Co^+ center bound to a neutral tpyPY2Me ligand, one-electron reductions of $[Fe]^{2+}$ and $[Ni]^{2+}$ involve a primarily ligand-centered event, resulting in $[Fe]^+$ and $[Ni]^+$ complexes with formal Fe^{2+} and Ni^{2+} centers bound to a reduced $(tpyPY2Me^{\bullet})^-$ ligand. It is noteworthy that a comparison of the first reduction events for the iron, cobalt, and nickel analogs exhibit a continuum of all three primary outcomes for reducing a transition metal complex bound to a redox non-innocent ligand: (1) a pure ligand-based reduction (Fe), (2) a pure metal-based reduction (Co), and (3) a ligand-based reduction with a large character of coupling between a metal d orbital and ligand π^* orbital, resulting in a broken symmetry configuration (Ni).

Despite the marked differences in electronic structure for the singly-reduced forms of the iron, cobalt, and nickel tpyPY2Me complexes, all three metals share similar electronic character upon introduction of a second reduction event. Comparing DFT results obtained for $[Co]^0$ (Figure 6, right) to those of $[Fe]^{0}$ [44] and $[Ni]^0$, [53] we observe that each first-row transition complex adopts a high-spin, unreduced formal M^{2+} center bound to a doubly-reduced $(tpyPY2Me^{\bullet\bullet})^{2-}$ ligand.

Thus, in the case of the second reduction event, the complexes differ only in the extent of d /π* orbital coupling between the metal atom and surrounding terpyridine ligand fragment.
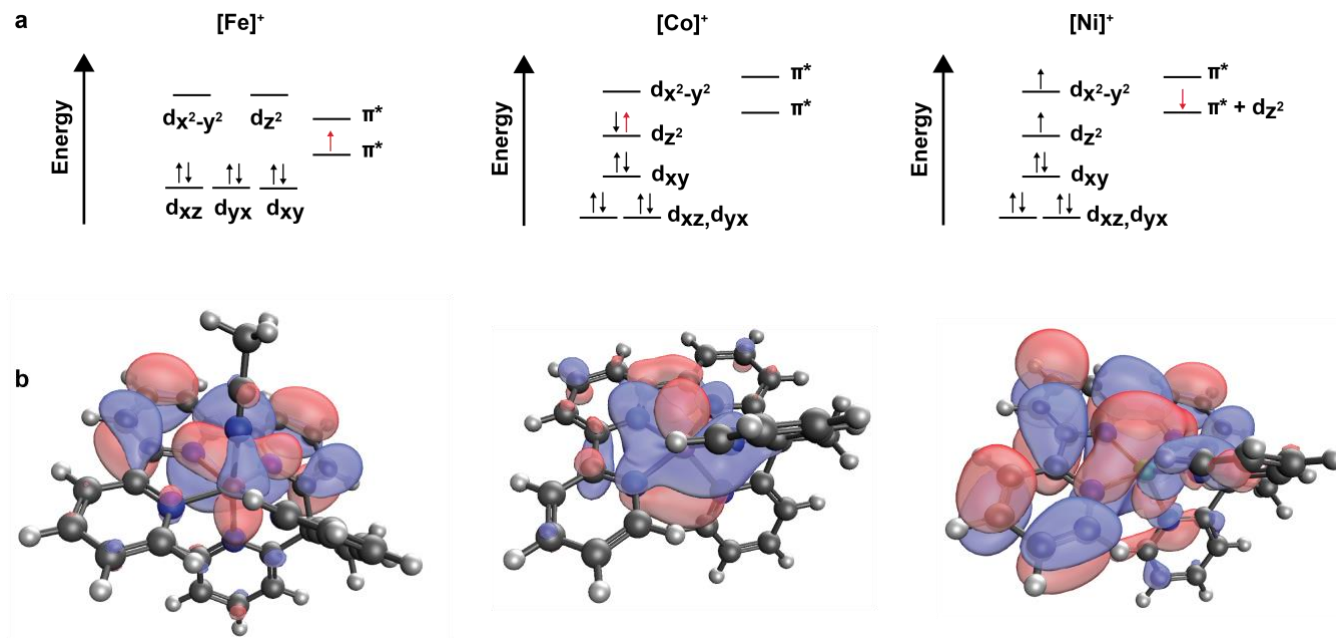
Figure 7. DFT analysis comparing varying metal-ligand redox behavior of iron, cobalt, and nickel metal centers bound to a redox non-innocent tpyPY2Me ligand framework upon one-electron reduction. For each complex the resulting first reduction of $[M]^{2+}$ to $[M]^+$ is shown with: (a) qualitative molecular orbital diagram consistent with DFT calculations, with newly added electrons highlighted in red; (b) relevant computed molecular orbitals. The results show that the one-electron reduction of $[Co]^{2+}$ is primarily metal-centered while the $[Fe]^{2+}$ and $[Ni]^{2+}$ analogs are ligand-centered.

CONCLUDING REMARKS

20

In summary, we have presented a comparative study of redox behavior for first-row transition metal complexes bearing the redox non-innocent ligand tpyPY2Me and applications of iron and cobalt congeners for photochemical CO$_2$RR. In particular, we established that the [Fe(tpyPY2Me)]$^{2+}$ (**[Fe]$^{2+}$**) complex is an extremely active and selective catalyst for photochemical reduction of CO$_2$ to CO, achieving up to 99% CO product selectivity with total turnover numbers (TON) and initial turnover frequencies (TOF) exceeding 30,000 and 900 min^{-1}, respectively. Electrochemical analysis shows that the **[Co]$^{2+}$** complex has a markedly higher thermodynamic barrier for reduction by two electrons compared to the **[Fe]$^{2+}$** analog, with a negative potential shift of 770 mV due to a large separation of the first and second reductions in the cobalt derivative. This difference in redox behavior is manifested in **[Co]$^{2+}$** showing lower activity, selectivity, and stability for electrochemical CO$_2$RR relative to **[Fe]$^{2+}$**, with electrode deposition and low faradaic efficiency observed during electrolysis for the former. These reactivity trends are mirrored in photochemical CO$_2$RR, where the **[Fe]$^{2+}$** system is 20-fold more active than the **[Co]$^{2+}$** congener under similar conditions. DLS analysis shows that photolysis of the cobalt system leads to formation of nanoparticles with loss of CO$_2$RR activity, whereas the iron system remains homogeneous, consistent with trends in electrochemical stability. Electronic structure calculations predict that the origin of the disparate redox behavior and catalysis observed for the **[Fe]$^{2+}$** and **[Co]$^{2+}$** complexes is the electronic configuration of the reduced species. Going from **[Co]$^{2+}$** to **[Co]$^+$**, a metal-centered spin density is predicted, which supports the observed loss in selectivity for CO$_2$RR and increased HER from a formal Co$^+$ species. Subsequent reduction of **[Co]$^+$** to **[Co]^0** is accompanied by a significant rearrangement of electrons to a metal-ligand coupling interaction in the form of an open-shell doublet with a formal Co^{2+} center bound to a doubly-reduced (tpyPY2Me$^{\bullet\bullet}$)$^{2-}$ ligand. Indeed, bulk electrolysis and photocatalysis experiments

21

suggest that this open-shell doublet **[Co]^0** species is catalytically competent for reduction of CO_2 to CO but is not a stable species, leading to inactive film or nanoparticle formation. In contrast, two-electron reduction to **[Fe]^0**, which bears an open-shell singlet electronic configuration driven by metal-ligand exchange coupling, proceeds at potentials that are nearly 800 mV more positive compared to the cobalt analog and shows high activity for both electrochemical and photochemical CO_2RR. This work highlights the value of metal-ligand exchange coupling as a design principle for tuning multielectron reactivity, presaging the use of this concept for advancing a broader array of catalytic transformations.

EXPERIMENTAL SECTION

Electrochemical Measurements

All electrochemical measurements were performed using a Bioanalytical Systems, Inc. (BASi) Epsilon potentiostat. Cyclic voltammetry (CV) data were measured in a three-electrode cell equipped with a glassy carbon disk (3.0 mm diameter) working electrode, platinum wire counter electrode, and a silver wire in a porous Vycor tip glass tube filled with electrolyte as a pseudo-reference electrode. The final concentration of **[Co]$^{2+}$** or **[Fe]$^{2+}$** catalyst was 1 mM. The working electrode was polished prior to each experiment with 0.05-micron alumina powder on a felt pad. The electrolyte was 0.1 M tetrabutylammonium hexafluorophosphate (TBAPF$_6$) in dry CH_3CN and sparged with either Ar or CO_2 as indicated. At the conclusion of each experiment, the pseudo-reference potentials were referenced against ferrocene/ferrocenium (Fc$^{0/+}$) used as an external standard. The scan rates for all cyclic voltammograms were 100 mV/s unless otherwise noted. All voltammograms were obtained with iR compensation. Controlled potential electrolysis

experiments were performed in a gastight PEEK electrolysis cell with a working compartment (12 mL liquid volume) and counter compartment (4 mL liquid volume) separated by an ultrafine glass frit. Either a 1 cm^2 glassy carbon plate (Tokai Carbon; Kanagawa, Japan) or a ~ 1 x 1 x 0.6 cm piece of 100 ppi (pores per linear inch) reticulated vitreous carbon foam (ERG Duocel; Oakland, CA) was used as the working electrode. A 2.5 cm diameter graphite planchet (Ted Pella; Redding, CA) was used as the auxiliary electrode, and an Ag wire in a Vycor tipped glass tube filled with electrolyte was used as a pseudo-reference electrode. The working compartment was filled with 12 mL of a 1 mM solution of catalyst dissolved in electrolyte (0.1 M NBu$_4$PF$_6$/CH$_3$CN) containing either 0.1 M or 1 M phenol as a proton source. The counter electrode chamber was filled with 4 mL of a 20 mM solution of tetrabutylammonium acetate dissolved in electrolyte. This soluble source of acetate was sacrificially oxidized to generate CO_2 and ethane, thereby preventing GC detection of solvent oxidation byproducts. Both compartments were sealed to be gastight. The working compartment was sparged with CO_2 for 10 min, then sealed and injected with 0.50 mL of ethane as a gaseous internal standard. A CV scan was collected prior to the CPE measurement to calibrate the potential. The electrolyte solution was constantly stirred during the CPE experiment with a 1 cm stir bar. At the conclusion of the experiment, the headspace was injected directly into an SRI-GC (model #8610C) equipped with 6' Hayesep D and 13X molecular sieve chromatographic columns. Two in-line detectors were used: a TCD for H_2 detection and an FID with a methanizer for $CO/CO_2/C_2H_6$ detection. Analytes of interest were quantified by comparing a ratios of analyte/internal stand peak integrals to a calibration curve with known amounts of analyte.

Photocatalytic CO$_2$ Reduction

Experiments were conducted inside a 25 mL borosilicate culture tube equipped with a stir bar, rubber septum, and aluminum crimped top. These reaction vessels contained 5 mL CH_3CN, 2 µM catalyst, 200 µM photosensitizer, 100 mM BIH (112 mg), and 1 M phenol (470 mg). The reaction tubes were sparged with CO_2 for 10 minutes, followed by injection of a gaseous internal standard (0.1 mL of C_2H_6). Reactions were placed on a stir plate 13 cm from two Kessil blue LED lamps (440 nm) for 15 or 30 minutes at a time and kept at ambient temperature with a fan. Analysis of the headspace by GC was conducted for product detection as described for above for CPE. Samples were then re-sparged with CO_2, and the process was repeated for the following timepoint of an experiment.

Computational Details

Density functional theory (DFT) calculations for free energies, reduction potentials and localized orbital bonding analysis (LOBA) oxidation state analysis were performed with the Q-Chem electronic structure package.[71] Geometry optimizations and frequency analysis were obtained using the ωB97X-D and a mixed basis set (def2-TZVP for metal Co center, def2-SVP for ligand main group elements). Solvation energies with CH_3CN solvent used to compute reduction potentials were approximated with single point calculations employing a C-PCM solvent model and the ωB97M- V functional with the def2-TZVP basis set for all atoms. Additional density functionals were probed, including similar range-separated hybrid functionals such as ωB97X-D and CAM-B3LYP, but all yielded substantially less agreement with experimental values (Table S5). The ferrocene/ferrocenium couple ($Fc^{0/+}$) was used as an internal standard for our reported reduction potentials. The $Fc^{0/+}$ couple was calculated with each reported density functional before standardizing to optimize potential error cancellation.

ASSOCIATED CONTENT

Supporting Information. Experimental and computational details, supplemental electrochemical and spectroscopic data, X-ray crystallography data, and DFT geometry optimized atomic xyz coordinates is available free of charge via the Internet at http://pubs.acs.org.

AUTHOR INFORMATION

Corresponding Author

*Christopher J. Chang – Departments of Chemistry and Molecular and Cell Biology University of California, Berkeley, CA, 94720, USA; Chemical Sciences Division, Lawrence Berkeley National Laboratory, Berkeley, CA, 94720, USA. orcid.org/0000-0001-5732-9497; Email: chrischang@berkeley.edu

Authors

Patricia De La Torre – Department of Chemistry University of California, Berkeley, CA, 94720, USA; Chemical Sciences Division, Lawrence Berkeley National Laboratory, Berkeley, CA, 94720, USA. orcid.org/0000-0002-3825-8010.

Jeffrey S. Derrick – Department of Chemistry University of California, Berkeley, CA, 94720, USA; Chemical Sciences Division, Lawrence Berkeley National Laboratory, Berkeley, CA, 94720, USA. orcid.org/0000-0002-3879-2897.

Andrew Snider – Department of Chemistry University of California, Berkeley, CA, 94720, USA; Chemical Sciences Division, Lawrence Berkeley National Laboratory, Berkeley, CA, 94720, USA. orcid.org/ 0000-0003-2322-3533.

Peter T. Smith – Department of Chemistry University of California, Berkeley, CA, 94720, USA; Chemical Sciences Division, Lawrence Berkeley National Laboratory, Berkeley, CA, 94720, USA. orcid.org/0000-0002-8892-3752.

Matthias Loipersberger – Department of Chemistry University of California, Berkeley, CA, 94720, USA. orcid.org/0000-0002-3648-0101.

Martin Head-Gordon – Department of Chemistry University of California, Berkeley, CA, 94720, USA; Chemical Sciences Division, Lawrence Berkeley National Laboratory, Berkeley, CA, 94720, USA. orcid.org/0000-0002-4309-6669.

ACKNOWLEDGMENTS

REFERENCES

1.   Sanz-Pérez, E. S.; Murdock, C. R.; Didas, S. A.; Jones, C. W., Direct Capture of CO_2 from Ambient Air. *Chemical Reviews* **2016,** *116* (19), 11840-11876.

2.   Hepburn, C.; Adlen, E.; Beddington, J.; Carter, E. A.; Fuss, S.; Mac Dowell, N.; Minx, J. C.; Smith, P.; Williams, C. K., The technological and economic prospects for CO_2 utilization and removal. *Nature* **2019,** *575* (7781), 87-97.

3.   Wang, Z. J.; Song, H.; Liu, H.; Ye, J., Coupling of Solar Energy and Thermal Energy for Carbon Dioxide Reduction: Status and Prospects. *Angewandte Chemie International Edition* **2020,** *59* (21), 8016-8035.

4.   Proppe, A. H.; Li, Y. C.; Aspuru-Guzik, A.; Berlinguette, C. P.; Chang, C. J.; Cogdell, R.; Doyle, A. G.; Flick, J.; Gabor, N. M.; van Grondelle, R.; Hammes-Schiffer, S.; Jaffer, S. A.; Kelley, S. O.; Leclerc, M.; Leo, K.; Mallouk, T. E.; Narang, P.; Schlau-Cohen, G. S.; Scholes, G. D.; Vojvodic, A.; Yam, V. W.-W.; Yang, J. Y.; Sargent, E. H., Bioinspiration in light harvesting and catalysis. *Nature Reviews Materials* **2020,** *5* (11), 828-846.

5.   Meyer, T. J., Chemical approaches to artificial photosynthesis. *Accounts of Chemical Research* **1989,** *22* (5), 163-170.

6.   Lewis, N. S.; Nocera, D. G., Powering the planet: Chemical challenges in solar energy utilization. *Proceedings of the National Academy of Sciences* **2006,** *103* (43), 15729-15735.

7.   Nocera, D. G., Chemistry of Personalized Solar Energy. *Inorganic Chemistry* **2009,** *48* (21), 10001-10017.

8.   Gray, H. B., Powering the planet with solar fuel. *Nature Chemistry* **2009,** *1* (1), 7-7.

9.   Morris, A. J.; Meyer, G. J.; Fujita, E., Molecular Approaches to the Photocatalytic Reduction of Carbon Dioxide for Solar Fuels. *Accounts of Chemical Research* **2009,** *42* (12), 1983-1994.

10.   Nocera, D. G., The Artificial Leaf. *Accounts of Chemical Research* **2012,** *45* (5), 767-776.

11.   Takeda, H.; Cometto, C.; Ishitani, O.; Robert, M., Electrons, Photons, Protons and Earth-Abundant Metal Complexes for Molecular Catalysis of CO_2 Reduction. *ACS Catalysis* **2016,** *7* (1), 70-88.

12.   Nocera, D. G., Solar Fuels and Solar Chemicals Industry. *Accounts of Chemical Research* **2017,** *50* (3), 616-619.

13.   Smith, P. T.; Nichols, E. M.; Cao, Z.; Chang, C. J., Hybrid Catalysts for Artificial Photosynthesis: Merging Approaches from Molecular, Materials, and Biological Catalysis. *Accounts of Chemical Research* **2020,** *53* (3), 575-587.

14.   Pannwitz, A.; Klein, D. M.; Rodríguez-Jiménez, S.; Casadevall, C.; Song, H.; Reisner, E.; Hammarström, L.; Bonnet, S., Roadmap towards solar fuel synthesis at the water interface of liposome membranes. *Chemical Society Reviews* **2021,** *50* (8), 4833-4855.

15.   Nocera, D. G., Proton-Coupled Electron Transfer: The Engine of Energy Conversion and Storage. *Journal of the American Chemical Society* **2022,** *144* (3), 1069-1081.

16.   Benson, E. E.; Kubiak, C. P.; Sathrum, A. J.; Smieja, J. M., Electrocatalytic and homogeneous approaches to conversion of CO_2 to liquid fuels. *Chemical Society Reviews* **2009,** *38* (1), 89-99.

17.   Rao, H.; Schmidt, L. C.; Bonin, J.; Robert, M., Visible-light-driven methane formation from CO_2 with a molecular iron catalyst. *Nature* **2017,** *548* (7665), 74-77.

18.   Call, A.; Cibian, M.; Yamamoto, K.; Nakazono, T.; Yamauchi, K.; Sakai, K., Highly Efficient and Selective Photocatalytic CO_2 Reduction to CO in Water by a Cobalt Porphyrin Molecular Catalyst. *ACS Catalysis* **2019,** *9* (6), 4867-4874.

19.   Wu, Y.;   Kim, D.; Teets, T. S., Photophysical Properties and Redox Potentials of Photosensitizers for Organic Photoredox Transformations. *Synlett* (EFirst).

20.   Yuan, H.; Cheng, B.; Lei, J.; Jiang, L.; Han, Z., Promoting photocatalytic CO_2 reduction with a molecular copper purpurin chromophore. *Nature Communications* **2021,** *12* (1), 1835.

21.   Leung, C.-F.; Lau, T.-C., Organic Photosensitizers for Catalytic Solar Fuel Generation. *Energy & Fuels* **2021,** *35* (23), 18888-18899.

22.   Stanley, P. M.; Haimerl, J.; Thomas, C.; Urstoeger, A.; Schuster, M.; Shustova, N. B.; Casini, A.; Rieger, B.; Warnan, J.; Fischer, R. A., Host–Guest Interactions in a Metal–Organic Framework Isoreticular Series for Molecular Photocatalytic CO_2 Reduction. *Angewandte Chemie International Edition* **2021,** *60* (33), 17854-17860.

23.   Zhang, X.; Cibian, M.; Call, A.; Yamauchi, K.; Sakai, K., Photochemical CO_2 Reduction Driven by Water-Soluble Copper(I) Photosensitizer with the Catalysis Accelerated by Multi-Electron Chargeable Cobalt Porphyrin. *ACS Catalysis* **2019,** *9* (12), 11263-11273.

24.   Cheung, P. L.; Kapper, S. C.; Zeng, T.; Thompson, M. E.; Kubiak, C. P., Improving Photocatalysis for the Reduction of CO_2 through Non-covalent Supramolecular Assembly. *Journal of the American Chemical Society* **2019,** *141* (38), 14961-14965.

25.   Arcudi, F.; Đorđević, L.; Nagasing, B.; Stupp, S. I.; Weiss, E. A., Quantum Dot-Sensitized Photoreduction of CO_2 in Water with Turnover Number > 80,000. *Journal of the American Chemical Society* **2021,** *143* (43), 18131-18138.

26.   Lian, S.; Kodaimati, M. S.; Weiss, E. A., Photocatalytically Active Superstructures of Quantum Dots and Iron Porphyrins for Reduction of CO_2 to CO in Water. *ACS Nano* **2018,** *12* (1), 568-575.

27.   Tamaki, Y.; Ishitani, O., Supramolecular Photocatalysts for the Reduction of CO_2. *ACS Catalysis* **2017,** *7* (5), 3394-3409.

28.   Yang, Z.-Z.; He, L.-N.; Gao, J.; Liu, A.-H.; Yu, B., Carbon dioxide utilization with C–N bond formation: carbon dioxide capture and subsequent conversion. *Energy & Environmental Science* **2012,** *5* (5), 6602-6639.

29.   Sampaio, R. N.; Grills, D. C.; Polyansky, D. E.; Szalda, D. J.; Fujita, E., Unexpected Roles of Triethanolamine in the Photochemical Reduction of CO_2 to Formate by Ruthenium Complexes. *Journal of the American Chemical Society* **2020,** *142* (5), 2413-2428.

30.   Bhattacharya, M.; Sebghati, S.; VanderLinden, R. T.; Saouma, C. T., Toward Combined Carbon Capture and Recycling: Addition of an Amine Alters Product Selectivity from CO to Formic Acid in Manganese Catalyzed Reduction of CO_2. *Journal of the American Chemical Society* **2020,** *142* (41), 17589-17597.

31.   Yamazaki, Y.; Miyaji, M.; Ishitani, O., Utilization of Low-Concentration CO_2 with Molecular Catalysts Assisted by CO_2-Capturing Ability of Catalysts, Additives, or Reaction Media. *Journal of the American Chemical Society* **2022,** *144* (15), 6640-6660.

32.   Bhattacharya, M.; Sebghati, S.; Vercella, Y. M.; Saouma, C. T., Electrochemical Reduction of Carbamates and Carbamic Acids: Implications for Combined Carbon Capture and Electrochemical CO_2 Recycling. *Journal of The Electrochemical Society* **2020,** *167* (8), 086507.

33.   Smieja, J. M.; Kubiak, C. P., Re(bipy-tBu)(CO)₃Cl−improved Catalytic Activity for Reduction of Carbon Dioxide: IR-Spectroelectrochemical and Mechanistic Studies. *Inorganic Chemistry* **2010,** *49* (20), 9283-9289.

34.   Thoi, V. S.; Chang, C. J., Nickel N-heterocyclic carbene–pyridine complexes that exhibit selectivity for electrocatalytic reduction of carbon dioxide over water. *Chemical Communications* **2011,** *47* (23), 6578-6580.

35.   Bourrez, M.; Molton, F.; Chardon-Noblat, S.; Deronzier, A., [Mn(bipyridyl)(CO)$_3$Br]: An Abundant Metal Carbonyl Complex as Efficient Electrocatalyst for CO_2 Reduction. *Angewandte Chemie International Edition* **2011,** *50* (42), 9903-9906.

36.   Thoi, V. S.; Kornienko, N.; Margarit, C. G.; Yang, P.; Chang, C. J., Visible-Light Photoredox Catalysis: Selective Reduction of Carbon Dioxide to Carbon Monoxide by a Nickel N-Heterocyclic Carbene–Isoquinoline Complex. *Journal of the American Chemical Society* **2013,** *135* (38), 14413-14424.

37.   Smieja, J. M.; Sampson, M. D.; Grice, K. A.; Benson, E. E.; Froehlich, J. D.; Kubiak, C. P., Manganese as a Substitute for Rhenium in CO_2 Reduction Catalysts: The Importance of Acids. *Inorganic Chemistry* **2013,** *52* (5), 2484-2491.

38.   Machan, C. W.; Chabolla, S. A.; Kubiak, C. P., Reductive Disproportionation of Carbon Dioxide by an Alkyl-Functionalized Pyridine Monoimine Re(I) fac-Tricarbonyl Electrocatalyst. *Organometallics* **2015,** *34* (19), 4678-4683.

39.   Guo, Z.; Cheng, S.; Cometto, C.; Anxolabehere-Mallart, E.; Ng, S. M.; Ko, C. C.; Liu, G.; Chen, L.; Robert, M.; Lau, T. C., Highly Efficient and Selective Photocatalytic CO_2 Reduction by Iron and Cobalt Quaterpyridine Complexes. *J Am Chem Soc* **2016,** *138* (30), 9413-6.

40.   Liyanage, N. P.; Dulaney, H. A.; Huckaba, A. J.; Jurss, J. W.; Delcamp, J. H., Electrocatalytic Reduction of CO_2 to CO With Re-Pyridyl-NHCs: Proton Source Influence on Rates and Product Selectivities. *Inorganic Chemistry* **2016,** *55* (12), 6085-6094.

41.   Elgrishi, N.; Chambers, M. B.; Wang, X.; Fontecave, M., Molecular polypyridine-based metal complexes as catalysts for the reduction of CO_2. *Chemical Society Reviews* **2017,** *46* (3), 761-796.

42.   Sung, S.; Kumar, D.; Gil-Sepulcre, M.; Nippe, M., Electrocatalytic CO_2 Reduction by Imidazolium-Functionalized Molecular Catalysts. *Journal of the American Chemical Society* **2017,** *139* (40), 13993-13996.

43.   Sung, S.; Li, X.; Wolf, L. M.; Meeder, J. R.; Bhuvanesh, N. S.; Grice, K. A.; Panetier, J. A.; Nippe, M., Synergistic Effects of Imidazolium-Functionalization on fac-Mn(CO)$_3$ Bipyridine Catalyst Platforms for Electrocatalytic Carbon Dioxide Reduction. *Journal of the American Chemical Society* **2019,** *141* (16), 6569-6582.

44.   Derrick, J. S.; Loipersberger, M.; Chatterjee, R.; Iovan, D. A.; Smith, P. T.; Chakarawet, K.; Yano, J.; Long, J. R.; Head-Gordon, M.; Chang, C. J., Metal–Ligand Cooperativity via Exchange Coupling Promotes Iron- Catalyzed Electrochemical CO_2 Reduction at Low Overpotentials. *Journal of the American Chemical Society* **2020,** *142* (48), 20489-20501.

45.   Qin, Y.; Chen, L.; Chen, G.; Guo, Z.; Wang, L.; Fan, H.; Robert, M.; Lau, T. C., A highly active and robust iron quinquepyridine complex for photocatalytic CO_2 reduction in aqueous acetonitrile solution. *Chem Commun (Camb)* **2020,** *56* (46), 6249-6252.

46.   Boutin, E.; Merakeb, L.; Ma, B.; Boudy, B.; Wang, M.; Bonin, J.; Anxolabéhère-Mallart, E.; Robert, M., Molecular catalysis of CO_2 reduction: recent advances and perspectives in electrochemical and light-driven processes with selected Fe, Ni and Co aza macrocyclic and polypyridine complexes. *Chemical Society Reviews* **2020,** *49* (16), 5772-5809.

47.   Gonell, S.; Lloret-Fillol, J.; Miller, A. J. M., An Iron Pyridyl-Carbene Electrocatalyst for Low Overpotential CO_2 Reduction to CO. *ACS Catalysis* **2021,** *11* (2), 615-626.

48.   Wang, X.-Z.; Meng, S.-L.; Chen, J.-Y.; Wang, H.-X.; Wang, Y.; Zhou, S.; Li, X.-B.; Liao, R.-Z.; Tung, C.-H.; Wu, L.-Z., Mechanistic Insights Into Iron(II) Bis(pyridyl)amine-Bipyridine Skeleton for Selective CO_2 Photoreduction. *Angewandte Chemie International Edition* **2021,** *60* (50), 26072-26079.

49.   Tsubonouchi, Y.; Takahashi, D.; Berber, M. R.; Mohamed, E. A.; Zahran, Z. N.; Alenad, A. M.; Althubiti, N. A.; Yagi, M., Highly selective electrocatalysis for carbon dioxide reduction to formic acid by a Co(II) complex with an equatorial N_4 ligand. *Electrochimica Acta* **2021,** *387*, 138545.

50.   Queyriaux, N., Redox-Active Ligands in Electroassisted Catalytic H^+ and CO_2 Reductions: Benefits and Risks. *ACS Catalysis* **2021,** *11* (7), 4024-4035.

51.   Loipersberger, M.; Cabral, D. G. A.; Chu, D. B. K.; Head-Gordon, M., Mechanistic Insights into Co and Fe Quaterpyridine-Based CO_2 Reduction Catalysts: Metal–Ligand Orbital Interaction as the Key Driving Force for Distinct Pathways. *Journal of the American Chemical Society* **2021,** *143* (2), 744-763.

52.   Nganga, J. K.; Wolf, L. M.; Mullick, K.; Reinheimer, E.; Saucedo, C.; Wilson, M. E.; Grice, K. A.; Ertem, M. Z.; Angeles-Boza, A. M., Methane Generation from CO_2 with a Molecular Rhenium Catalyst. *Inorganic Chemistry* **2021,** *60* (6), 3572-3584.

53.   Wuttig, A.; Derrick, J. S.; Loipersberger, M.; Snider, A.; Head-Gordon, M.; Chang, C. J.; Toste, F. D., Controlled Single-Electron Transfer via Metal–Ligand Cooperativity Drives Divergent Nickel-Electrocatalyzed Radical Pathways. *Journal of the American Chemical Society* **2021,** *143* (18), 6990-7001.

54.   Chan, S. L.-F.; Lam, T. L.; Yang, C.; Yan, S.-C.; Cheng, N. M., A robust and efficient cobalt molecular catalyst for CO_2 reduction. *Chemical Communications* **2015,** *51* (37), 7799-7801.

55.   Roy, S.; Sharma, B.; Pécaut, J.; Simon, P.; Fontecave, M.; Tran, P. D.; Derat, E.; Artero, V., Molecular Cobalt Complexes with Pendant Amines for Selective Electrocatalytic Reduction of Carbon Dioxide to Formic Acid. *Journal of the American Chemical Society* **2017,** *139* (10), 3685-3696.

56.   Zhang, L.; Li, S.; Liu, H.; Cheng, Y.-S.; Wei, X.-W.; Chai, X.; Yuan, G., Highly Efficient and Selective Visible-Light Driven CO_2 Reduction by Two Co-Based Catalysts in Aqueous Solution. *Inorganic Chemistry* **2020,** *59* (23), 17464-17472.

57.   Chen, X.; Wei, Y.; Sun, W.; Meng, X.; Hao, S.; Gao, Y., Turning off hydrogen evolution via an organic dye photosensitizer in aqueous acetonitrile solution during photocatalytic CO_2 reduction to CO. *Molecular Catalysis* **2021,** *500*, 111299.

58.   Sun, Y.; Bigi, J. P.; Piro, N. A.; Tang, M. L.; Long, J. R.; Chang, C. J., Molecular Cobalt Pentapyridine Catalysts for Generating Hydrogen from Water. *Journal of the American Chemical Society* **2011,** *133* (24), 9212-9215.

59.   Kilner, C. A.; Halcrow, M. A., An unusual discontinuity in the thermal spin transition in [Co(terpy)$_2$][BF$_4$]$_2$. *Dalton Transactions* **2010,** *39* (38), 9008-9012.

60.   England, J.; Bill, E.; Weyhermüller, T.; Neese, F.; Atanasov, M.; Wieghardt, K., Molecular and Electronic Structures of Homoleptic Six-Coordinate Cobalt(I) Complexes of 2,2′:6′,2″-Terpyridine, 2,2′-Bipyridine, and 1,10-Phenanthroline. An Experimental and Computational Study. *Inorganic Chemistry* **2015,** *54* (24), 12002-12018.

61.   Hamann, T. W., The end of iodide? Cobalt complex redox shuttles in DSSCs. *Dalton Transactions* **2012,** *41* (11), 3111-3115.

62.   Kashif, M. K.; Axelson, J. C.; Duffy, N. W.; Forsyth, C. M.; Chang, C. J.; Long, J. R.; Spiccia, L.; Bach, U., A New Direction in Dye-Sensitized Solar Cells Redox Mediator Development: In Situ Fine-Tuning of the Cobalt(II)/(III) Redox Potential through Lewis Base Interactions. *Journal of the American Chemical Society* **2012,** *134* (40), 16646-16653.

63.   Giribabu, L.; Bolligarla, R.; Panigrahi, M., Recent Advances of Cobalt(II/III) Redox Couples for Dye-Sensitized Solar Cell Applications. *The Chemical Record* **2015,** *15* (4), 760-788.

64.   Nippe, M.; Khnayzer, R. S.; Panetier, J. A.; Zee, D. Z.; Olaiya, B. S.; Head-Gordon, M.; Chang, C. J.; Castellano, F. N.; Long, J. R., Catalytic proton reduction with transition metal complexes of the redox-active ligand bpy2PYMe. *Chemical Science* **2013,** *4* (10), 3934-3945.

65.   Guo, Z.; Yu, F.; Yang, Y.; Leung, C.-F.; Ng, S.-M.; Ko, C.-C.; Cometto, C.; Lau, T.-C.; Robert, M., Photocatalytic Conversion of CO_2 to CO by a Copper(II) Quaterpyridine Complex. *ChemSusChem* **2017,** *10* (20), 4009-4013.

66.   Rao, H.; Lim, C.-H.; Bonin, J.; Miyake, G. M.; Robert, M., Visible-Light-Driven Conversion of CO_2 to CH_4 with an Organic Sensitizer and an Iron Porphyrin Catalyst. *Journal of the American Chemical Society* **2018,** *140* (51), 17830-17834.

67.   Durham, B.; Caspar, J. V.; Nagle, J. K.; Meyer, T. J., Photochemistry of tris(2,2'-bipyridine)ruthenium(2+) ion. *Journal of the American Chemical Society* **1982,** *104* (18), 4803-4810.

68.   Khnayzer, R. S.; Olaiya, B. S.; El Roz, K. A.; Castellano, F. N., Homogeneous Photocatalytic H_2 Production Using a RuII Bathophenanthroline Metal-to-Ligand Charge-Transfer Photosensitizer. *ChemPlusChem* **2016,** *81* (10), 1090-1097.

69.   Gong, L.; Wang, J.; Li, H.; Wang, L.; Zhao, J.; Zhu, Z., Acriflavine–cobaloxime–triethanolamine homogeneous photocatalytic system for water splitting and the multiple effects of cobaloxime and triethanolamine. *Catalysis Communications* **2011,** *12* (12), 1099-1103.

70.   Yuan, Y.-J.; Yu, Z.-T.; Chen, D.-Q.; Zou, Z.-G., Metal-complex chromophores for solar hydrogen generation. *Chemical Society Reviews* **2017,** *46* (3), 603-631.

71.   Epifanovsky, E.; Gilbert, A. T. B.; Feng, X.; Lee, J.; Mao, Y.; Mardirossian, N.; Pokhilko, P.; White, A. F.; Coons, M. P.; Dempwolff, A. L.; Gan, Z.; Hait, D.; Horn, P. R.; Jacobson, L. D.; Kaliman, I.; Kussmann, J.; Lange, A. W.; Lao, K. U.; Levine, D. S.; Liu, J.; McKenzie, S. C.; Morrison, A. F.; Nanda, K. D.; Plasser, F.; Rehn, D. R.; Vidal, M. L.; You, Z.-Q.; Zhu, Y.; Alam, B.; Albrecht, B. J.; Aldossary, A.; Alguire, E.; Andersen, J. H.; Athavale, V.; Barton, D.; Begam, K.; Behn, A.; Bellonzi, N.; Bernard, Y. A.; Berquist, E. J.; Burton, H. G. A.; Carreras, A.; Carter-Fenk, K.; Chakraborty, R.; Chien, A. D.; Closser, K. D.; Cofer-Shabica, V.; Dasgupta, S.; Wergifosse, M. d.; Deng, J.; Diedenhofen, M.; Do, H.; Ehlert, S.; Fang, P.-T.; Fatehi, S.; Feng, Q.; Friedhoff, T.; Gayvert, J.; Ge, Q.; Gidofalvi, G.; Goldey, M.; Gomes, J.; González-Espinoza, C. E.; Gulania, S.; Gunina, A. O.; Hanson-Heine, M. W. D.; Harbach, P. H. P.; Hauser, A.; Herbst, M. F.; Vera, M. H.; Hodecker, M.; Holden, Z. C.; Houck, S.; Huang, X.; Hui, K.; Huynh, B. C.; Ivanov, M.; Jász, Á.; Ji, H.; Jiang, H.; Kaduk, B.; Kähler, S.; Khistyaev, K.; Kim, J.; Kis, G.; Klunzinger, P.; Koczor-Benda, Z.; Koh, J. H.; Kosenkov, D.; Koulias, L.; Kowalczyk, T.; Krauter, C. M.; Kue, K.; Kunitsa, A.; Kus, T.; Ladjánszki, I.; Landau, A.; Lawler, K. V.; Lefrancois, D.; Lehtola, S.; Li, R. R.; Li, Y.-P.; Liang, J.; Liebenthal, M.; Lin, H.-H.; Lin, Y.-S.; Liu, F.; Liu, K.-Y.; Loipersberger, M.; Luenser, A.; Manjanath, A.; Manohar, P.; Mansoor, E.; Manzer, S. F.; Mao, S.-P.; Marenich, A. V.; Markovich, T.; Mason, S.; Maurer, S. A.; McLaughlin, P. F.; Menger, M. F. S. J.; Mewes, J.-M.; Mewes, S. A.; Morgante, P.; Mullinax, J. W.; Oosterbaan, K. J.; Paran, G.; Paul, A. C.; Paul, S. K.; Pavošević, F.; Pei, Z.; Prager, S.; Proynov, E. I.; Rák, Á.; Ramos-Cordoba, E.; Rana, B.; Rask, A. E.; Rettig, A.; Richard, R. M.; Rob, F.; Rossomme, E.; Scheele, T.; Scheurer, M.; Schneider, M.; Sergueev, N.; Sharada, S. M.; Skomorowski, W.; Small, D. W.; Stein, C. J.; Su, Y.-C.; Sundstrom, E. J.; Tao, Z.; Thirman, J.; Tornai, G. J.; Tsuchimochi, T.; Tubman, N. M.; Veccham, S. P.; Vydrov, O.; Wenzel, J.; Witte, J.; Yamada, A.; Yao, K.; Yeganeh, S.; Yost, S. R.; Zech, A.; Zhang, I. Y.; Zhang, X.; Zhang, Y.; Zuev, D.; Aspuru-Guzik, A.; Bell, A. T.; Besley, N. A.; Bravaya, K. B.; Brooks, B. R.; Casanova, D.; Chai, J.-

D.; Coriani, S.; Cramer, C. J.; Cserey, G.; DePrinceIII, A. E.; DiStasioJr., R. A.; Dreuw, A.; Dunietz, B. D.; Furlani, T. R.; GoddardIII, W. A.; Hammes-Schiffer, S.; Head-Gordon, T.; Hehre, W. J.; Hsu, C.-P.; Jagau, T.-C.; Jung, Y.; Klamt, A.; Kong, J.; Lambrecht, D. S.; Liang, W.; Mayhall, N. J.; McCurdy, C. W.; Neaton, J. B.; Ochsenfeld, C.; Parkhill, J. A.; Peverati, R.; Rassolov, V. A.; Shao, Y.; Slipchenko, L. V.; Stauch, T.; Steele, R. P.; Subotnik, J. E.; Thom, A. J. W.; Tkatchenko, A.; Truhlar, D. G.; Voorhis, T. V.; Wesolowski, T. A.; Whaley, K. B.; WoodcockIII, H. L.; Zimmerman, P. M.; Faraji, S.; Gill, P. M. W.; Head-Gordon, M.; Herbert, J. M.; Krylov, A. I., Software for the frontiers of quantum chemistry: An overview of developments in the Q-Chem 5 package. *The Journal of Chemical Physics* **2021,** *155* (8), 084801.